Journal of Molecular Structure 1281 (2023) 135157

Contents lists available at ScienceDirect

Journal of Molecular Structure

journal homepage: www.elsevier.com/locate/molstr

Structural, physicochemical and anticancer study of Zn complexes with pyridyl-based thiazolyl-hydrazones

Jovana B. Araškov[a], Natalia Maciejewska[b], Mateusz Olszewski[b], Aleksandar Višnjevac[c], Vladimir Blagojević[d], Henrique S. Fernandes[e,f], Sérgio F. Sousa[e,f], Adrián Puerta[g], José M. Padrón[g], Berta Barta Holló[h], Miguel Monge[i], María Rodríguez-Castillo[i], José M. López-de-Luzuriaga[i], Özlem Uğuz[j], Atıf Koca[j], Tamara R. Todorović[a], Nenad R. Filipović[k,*]

[a] University of Belgrade, Faculty of Chemistry, Studentski trg 12-16, Belgrade 11000, Serbia
[b] Department of Pharmaceutical Technology and Biochemistry, Faculty of Chemistry, Gdansk University Technology, Narutowicza 11/12, Gdansk 80-233, Poland
[c] Division of Physical Chemistry, Institute Ruđer Bošković, Bijenička cesta 54, Zagreb 10000, Croatia
[d] TBP Soft, Solunska 11, Belgrade 11000, Serbia
[e] UCIBIO – Applied Molecular Biosciences Unit, BioSIM – Department of Biomedicine, Faculty of Medicine, University of Porto, Porto 4200-319, Portugal
[f] Associate Laboratory i4HB – Institute for Health and Bioeconomy, Faculty of Medicine, University of Porto, Porto 4200-319, Portugal
[g] BioLab, Instituto Universitario de Bio-Orgánica "Antonio González", Universidad de La Laguna, La Laguna 38071, Spain
[h] University of Novi Sad, Faculty of Sciences, Trg Dositeja Obradovića 4, Novi Sad 21000, Serbia
[i] Departamento de Química, Universidad de La Rioja, Centro de Investigación en Síntesis Química (CISQ), Complejo Científico-Tecnológico, Logroño 26004, Spain
[j] Marmara University, Engineering Faculty, Department of Chemical Engineering, Goztepe, Istanbul 34722, Turkey
[k] University of Belgrade, Faculty of Agriculture, Nemanjina 6, Belgrade 11000, Serbia

ARTICLE INFO

Article history:
Received 16 November 2022
Revised 31 January 2023
Accepted 12 February 2023
Available online 15 February 2023

Keywords:
Intermolecular interactions
Photoluminescence
TD-DFT
Spectroelectrochemistry
Anticancer activity

ABSTRACT

Thiazolyl-hydrazones (THs) exhibit a wide spectrum of biological activity that can be enhanced by complexation with various metal ions. Zn(II) complexes with α-pyridine-1,3-TH ligands may represent an alternative to the standard platinum-based chemotherapeutics. In addition, they show photoluminescence properties and thus can be regarded as multifunctional materials. In this study, we synthesized and characterized three neutral Zn(II) complexes (**1**–**3**) with pyridine-based TH ligands HLS^{1-3} in order to investigate the influence of the ligands charge on the structure and intermolecular interactions in the solid state, and consequently photophysical properties. The deprotonation of the ligands mainly affects the relative energies of electronic levels in the complexes, compared to cationic counterparts, resulting in similar photoluminescence mechanisms and quantum yields with a small shift in emission energy. The influence of the substitution at the ligands' periphery on the selected quantum molecular descriptors of the complexes is localized to the substitution site. Also, the substituents did not considerably influence the redox responses of the complexes. However, predominant spectral changes were observed in the course of the first reduction and oxidation processes which caused distinct spectral color changes indicating their possible functionality for electrochromic applications. In addition, complex **1** showed antiproliferative activity with GI_{50} values below 2 μM on all tested cancer cell lines.

1. Introduction

1,3-Thiazolyl-hydrazones (1,3-THs; Fig. 1A) are compounds based on thiazolyl and hydrazone pharmacophores that exhibit a wide spectrum of pharmacological activities. 1,3-THs are known as a potent anti-inflammatory, antimicrobial, anticancer and antiparasitic agents [1]. Their ability to inhibit acetylcholinesterase and monoamine oxidases A and B indicates a possible use in neurodegenerative disease therapy, while their targeting properties towards α-glucosidase and α-amylase point to a potential for the treatment of type-2 diabetes mellitus [1,2]. Additionally, 1,3-THs are known to inhibit other biologically relevant enzymes such as 5′-

* Corresponding author.
E-mail address: nenadf@agrif.bg.ac.rs (N.R. Filipović).

https://doi.org/10.1016/j.molstruc.2023.135157
0022-2860/

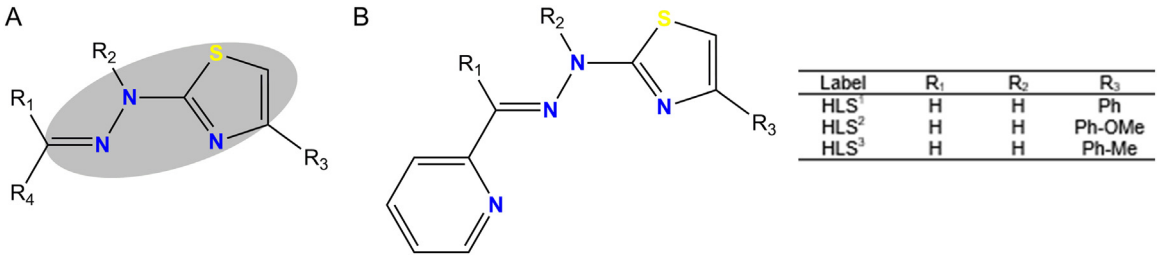

Fig. 1. (A) The general formula of 1,3-THs; (B) The general formula of the α-py-1,3-TH ligands HLS^{1-3} used in this study.

nucleotidase, β-glucuronidase, intestinal alkaline phosphatase and tissue non-specific alkaline phosphatase [1], as well as urease [3], cyclin-dependent kinase 2 [4], epidermal growth factor receptor tyrosine kinase [5], aldose reductase [6], matrix metalloproteinases MMP-2 and MMP-9 [7] and β-ketoacyl-ACP synthase [8].

Besides very potent and versatile biological effects, THs represent a class of, at least, bidentate ligand systems. Complexation of 1,3-THs with d-metals often results in enhancement of the biological activity of the complexes in comparison to the corresponding metal-free ligands [9,10]. Our studies are focused on 1,3-THs ligands that possess a pyridine substituent in α-position (α-py-1,3-THs, HLS^{1-3}, Fig. 1B). These ligands were designed to have the same donor set of atoms and to differ only in substitution at the ligand periphery. A single crystal X-ray diffraction analysis (XRD) study confirmed that this class of ligands coordinates in NNN tridentate manner *via* pyridine, imine and thiazole nitrogen atoms [11–14]. Again, the complexation of HLS^{1-3} with Co(III), Cd(II) and Zn(II) resulted in a synergistic effect regarding biological activity [11–15]. Co(III) complex with HLS^3 ligand, $[Co(LS^3)_2]BF_4$, appeared to have significant activity against *Pseudomonas aeruginosa*. Detailed experimental studies, supported by docking simulations, revealed that this compound inhibits *P. aeruginosa* 3-oxo-C12-HSL-dependent QS system (LasI/LasR system) *via* inhibition of transcriptional activator protein complex LasR-3-oxo-C12-HSL [15]. Studies of the anticancer potential of this compound showed that it reached the same level of inhibition of 3-D human mammary adenocarcinoma (MCF-7) spheroids as cisplatin. Our findings indicated that $[Co(LS^3)_2]BF_4$ has a different mode of activity in comparison to cisplatin and it can be suitable for combinational therapy [11]. Octahedral cationic Cd(II) and Zn(II) complexes of HLS^{1-3} appeared to be more active against several cancer cell lines when compared to cisplatin and 5-fluorouracil (5-FU), with GI_{50} values below 2 and 4 μM, respectively [13,14].

Zn(II) complexes gained much attention in recent years as possible alternatives to standard platinum-based chemotherapeutics [16,17]. In that respect, the antiproliferative activity of Zn(II) complexes with various types of α-py-1,3-TH ligands [18–21], including our most recent study [14], has been reported. Also, due to zero crystal field stabilization energy and the absence of potential quenching processes caused by d-d transitions, Zn(II) complexes may represent a cheaper alternative to other known luminescent materials [22,23].

To further investigate the influence of the ligands charge on the structure, intermolecular interactions in the solid state, and consequently photophysical properties, we have synthesized neutral Zn(II) complexes with α-py-1,3-TH ligands HLS^{1-3}. We conducted detailed studies of the redox mechanisms of obtained complexes with the voltammetric and *in-situ* spectroelectrochemical analysis to evaluate their potential for electrochromic applications. Soluble complex with HLS^1 has also been subjected to a detailed mechanistic study of its anticancer activity. Since the mechanism of biological activity depends on the chemical reactivity of compounds, quantum molecular descriptors related to the reported complexes' reactivity and bonding nature have been calculated.

2. Experimental

2.1. Materials and methods

The Supplementary material contains all details regarding materials and methods (Section 1).

2.2. Synthesis

The synthesis of the ligands HLS^{1-3} (Fig. 1B) was carried out by the literature protocol [12]. Details regarding the synthesis and characterization of complexes $[Zn(LS^1)_2]$ (**1**), $[Zn(LS^2)_2]$ (**2**), and $[Zn(LS^3)_2]$ (**3**) are given in Supplementary material (Section 1).

2.3. Characterization methods, computational details, electrochemical, anticancer, and photophysical study

Supplementary material (Section 1) contains experimental data for single crystal and powder diffraction X-ray analysis, Hirshfeld analysis, the energy distribution of intermolecular interactions, molecular electrostatic potential maps (MEP), Fukui functions, average local ionization energy (ALIE), QTAIM analysis, thermal analysis, electrochemistry, and *in situ* spectroelectrochemistry, anticancer activity, photophysical study, and details regarding DFT and TD-DFT calculations.

3. Results and discussion

3.1. General

Complex **1** was obtained by direct reaction of HLS^1 and $Zn(ClO_4)_2{\cdot}6H_2O$ in MeOH with the addition of KOH as a base and precipitating reagent for perchlorates. The synthesis of complexes **2** and **3** was carried out by a direct reaction starting from $Zn(CH_3COO)_2{\cdot}2H_2O$ with the ligand $HLS^{2/3}$ in MeOH, where the acetate ion served as a base. Molar conductivity measurements in DMSO showed that all the complexes are non-electrolytes. The IR spectra of the ligands contain characteristic bands around 3100 cm^{-1} which can be attributed to ν(N–H). The absence of these bands indicates that the ligands are coordinated in an anionic form. In addition, absence of the bands of stretching O–H vibrations in the range 3600–3200 cm^{-1} in spectrum of **1** indicates the absence of crystalline water or methanol molecules. Bands in the range 1609–1597 cm^{-1} and 1569–1573 cm^{-1}, which are assigned to the ν(C = N) of azomethine group and thiazole ring of the ligands, respectively, are significantly shifted to the lower frequencies in the spectra of the complexes (~1475 cm^{-1} and 1400 cm^{-1}, respectively). 1D (^{1}H and ^{13}C) NMR spectra of all complexes and 2D (^{1}H–^{13}C HSQC, ^{1}H–^{13}C HMBC, NOESY, and COZY) NMR spectra of **1** were recorded in DMSO–d_6 (all spectra are given in Supplementary material, Section 2). The differences between the ^{1}H and ^{13}C NMR spectra of the complexes and the corresponding ligands are significant. The absence of a signal at 12 ppm in the spectra of the complexes, derived from the N–H proton, indicates that the ligands

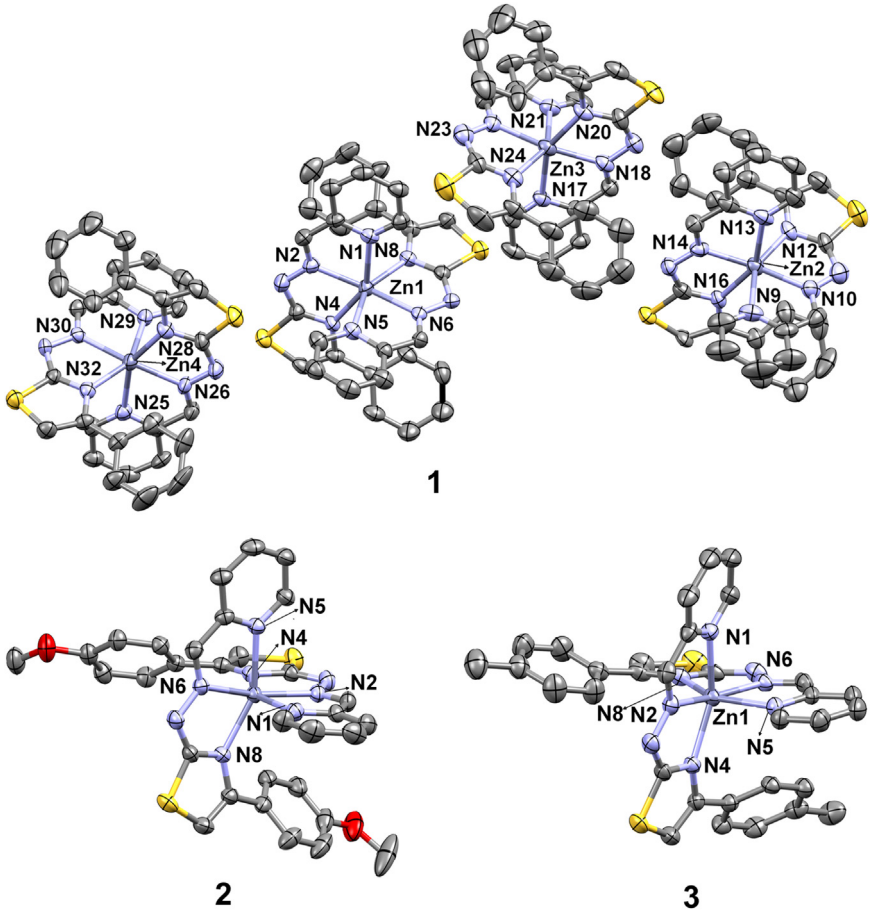

Fig. 2. ORTEP drawings of molecular structures of **1–3** with the labeled ligator atoms. Thermal ellipsoids are at a 30% probability level. Hydrogen atoms are omitted for clarity.

are coordinated in deprotonated form. Due to the deprotonation of N–H proton of the coordinated ligands, upfield shifts of all protons in ^{1}H NMR spectra of the complexes were observed. Shifts of almost all signals in ^{13}C NMR spectra of the complexes are also observed. Based on spectroscopic data, elemental analysis, and crystallographic data (*vide infra*), the general formula of the complexes $[Zn(LS^{1-3})_2]$ can be derived.

3.2. Molecular structures

ORTEP drawings of molecular structures of **1–3** are shown in Fig. 2. Bond distances and angles within the coordination sphere of the complexes are given in Tables S2–S5 (Section 3, Supplementary material). The asymmetric unit of **1** consists of four chemically identical but crystallographically different complex molecules (Tables S2 and S4, Supplementary material). Both **2** and **3** crystallize with one molecule in the asymmetric unit. In all complexes **1–3**, Zn(II) coordinates two deprotonated HLS^{1-3} ligands giving the distorted octahedral bischelate complexes, where ligator atoms are pyridine, azomethine and thiazole nitrogen atoms. The angular distortions of octahedral geometry in **1–3** exist due to the constraining influence of the ligands, which is a consequence of the position of the ligator atoms (Tables S4 and S5, Supplementary material).

3.3. Crystal packing analysis

Pairs of neighboring molecules were generated using the crystallographic structures of **1–3** to obtain all possible intermolecular interactions within each crystal. Interaction energies for each crystal structure were computed by single-point energy calculations. Illustrations of orientations, corresponding interactions and interaction energies (in kcal/mol), used to describe the packing in the crystal structure of **1–3** are given in Supplementary material (Section 3, Tables S6-S8). For a deeper understanding of intermolecular interactions, which govern the crystal packings of all complexes, a Hirshfeld surface analysis (HSA) was performed [24–26]. The Hirshfeld surfaces and 2D pseudosymmetric fingerprint plots of **1–3** are shown in Figures S16 and S17 (Supplementary material). The relative contributions of different types of interactions in all complexes are shown in Table 1. In the crystal packing of all complexes, C···H interactions have a high contribution. Although N···H interactions have a significantly lower contribution, they also represent the closest contacts seen as red spots on Hirshfeld sur-

Table 1
The surface area included in the selected intermolecular interactions (%).

Label of interaction		1	2	3	4	5
Type of interaction		H···C	H···N	H···S	C···C	O···H
1-Zn1	Surface	31.7	8.1	10.5	2.5	–
1-Zn2	area	25	9.4	11.5	3	–
1-Zn3	in-	25.6	9.9	10.1	3.6	–
1-Zn4	cluded	31.1	8.4	9.3	2.4	–
2	(%)	27.9	8.6	11.6	2	6.4
3		25.3	7.9	13	4.2	–

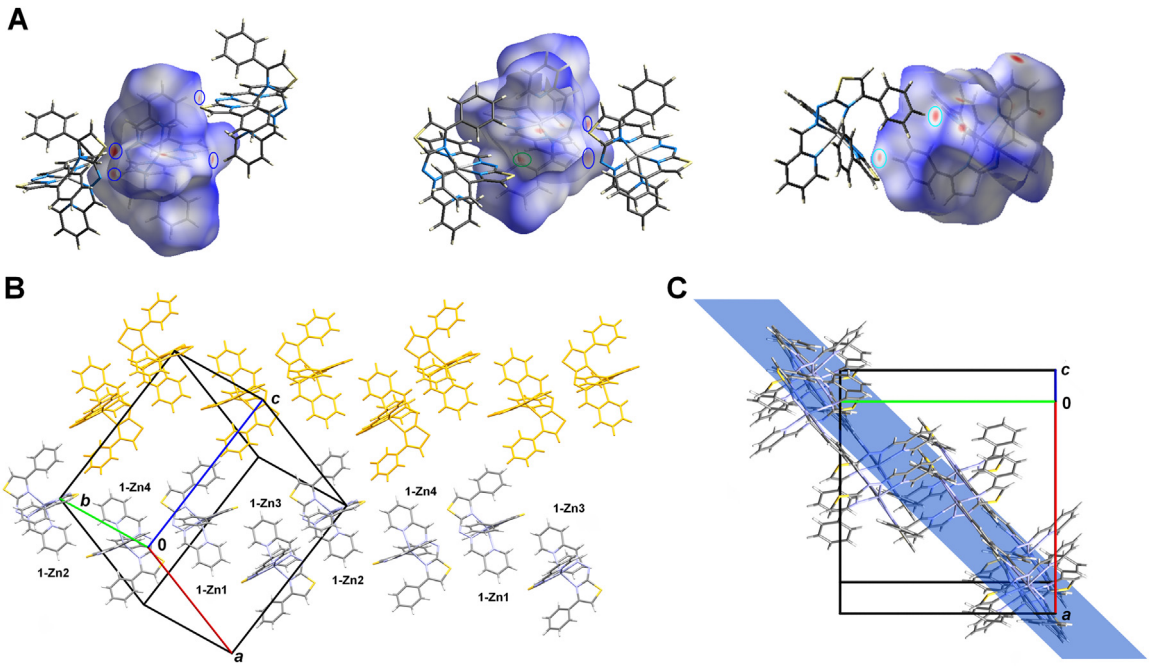

Fig. 3. (A) Different views of Hirshfeld surfaces displaying the pairwise N···H and S···H close contacts responsible for the formation of 2-D layers in the crystal packing of **1**. (B) 1-D chains running along the [2–21] crystallographic direction. (C) 2-D crystallographic layer parallel to the (110) plane in the crystal packing of **1**.

faces (Table 1 and Fig. 3 Figures S18 and S19, Supplementary material).

Since the asymmetric unit of **1** consists of four crystallographically different complex molecules, this implies the realization of different types of interactions, where each molecule of **1** will have a unique Hirshfeld surface (Figure S16, Supplementary material). Consequently, a direct comparison can be made between crystallographically different molecules of the complex. There are pairs of complex units (**1**-Zn1 and **1**-Zn4; **1**-Zn2 and **1**-Zn3) that have approximately similar contributions of the corresponding interactions. In the crystal packing of **1**, the most significant intermolecular interaction is the one where a deprotonated nitrogen atom from one complex molecule interacts with an aromatic proton from neighboring molecules (Fig. 3A). This interaction is responsible for the formation of the tetramer. **1**-Zn2 and **1**-Zn3 molecules additionally form bifurcated C□□□A (A = N and S) interactions which are responsible for the interconnection of tetramers in 1-D chain along the [2–21] crystallographic direction (Fig. 3B). 1-D chains are connected into 2-D layers parallel to the (110) crystallographic plane (Fig. 3C).

The crystal structure of **2** is based mainly on the non-classical hydrogen and aromatic interactions. CH···π and CH···N interactions are responsible for the formation of 1-D chains which are further connected into 2-D layers, parallel to the (101) crystallographic plane, via CH···S and π···π interactions. Additionally, these 2-D layers are connected via CH···O and CH···π interactions into a 3-D supramolecular structure (Figure S18, Supplementary material).

The crystal structure of **3** is also based mainly on the non-classical hydrogen and aromatic interactions (Figure S19, Supplementary material). The *zig-zag* 1-D chains are formed by CH···S, CH···π and H···H interactions. 1-D chains are interconnected through π···π and H···H interactions with the formation of 2-D layers parallel to the (102) crystallographic plane. Additional connections of these 2-D layers via CH···N, CH···S, CH···π, π···π, S···π and H···H interactions are responsible for 3-D supramolecular structure of **3**.

The Hirshfeld analysis of all three crystal structures revealed that slight differences in the nature of substituents at the ligands' periphery do not affect the distribution of the same type of intermolecular interactions. However, the ligands' periphery has a significant effect on the overall crystal structures since the complexes crystallize in different space groups (Table S1, Supplementary material).

3.4. X-ray powder diffraction analysis

Before the investigation of potential applications, the phase purity of the synthesized complexes was checked by PXRD. Rietveld refinement was performed using the crystal structures obtained by single crystals X-ray diffraction analysis (Figure S20, Supplementary material). It was shown that all the samples are phase pure. Powder XRD analysis was also used to determine the microstructural parameters of the complexes' powders (Table S9, Supplementary material). Preferred orientation using the Rietveld-Toraya model shows that all three complexes exhibit G1 values < 1, which are associated with platelet-like crystallites. This can be correlated with the existence of 2-D planes in the crystal packing of the complexes. The effect is much more pronounced in **1** and **2**. Crystallite size analysis shows that **3** exhibits relatively symmetrical crystallites, while crystallites of **1** and **2** are much more asymmetrical, with larger values along the *a, c* and *b* axes respectively. This is consistent with observed preferential orientation results. All complexes also exhibit a relatively small amount of microstrain in the structure, typically below 1%.

3.5. Local reactivity and bonding in 1–3

To computationally characterize complexes **1**–**3**, several quantum molecular descriptors related to their reactivity and bonding nature are calculated. ALIE and MEP are important quantum molecular properties descriptors related to electron density that provide a deeper understanding of the local reactive properties of molecules. MEP values are important in drug design and identification of the nucleophilic and electrophilic regions in molecules. Since ALIE represents the energy required for taking an electron from the molecule, it is used to recognize the molecular sites that

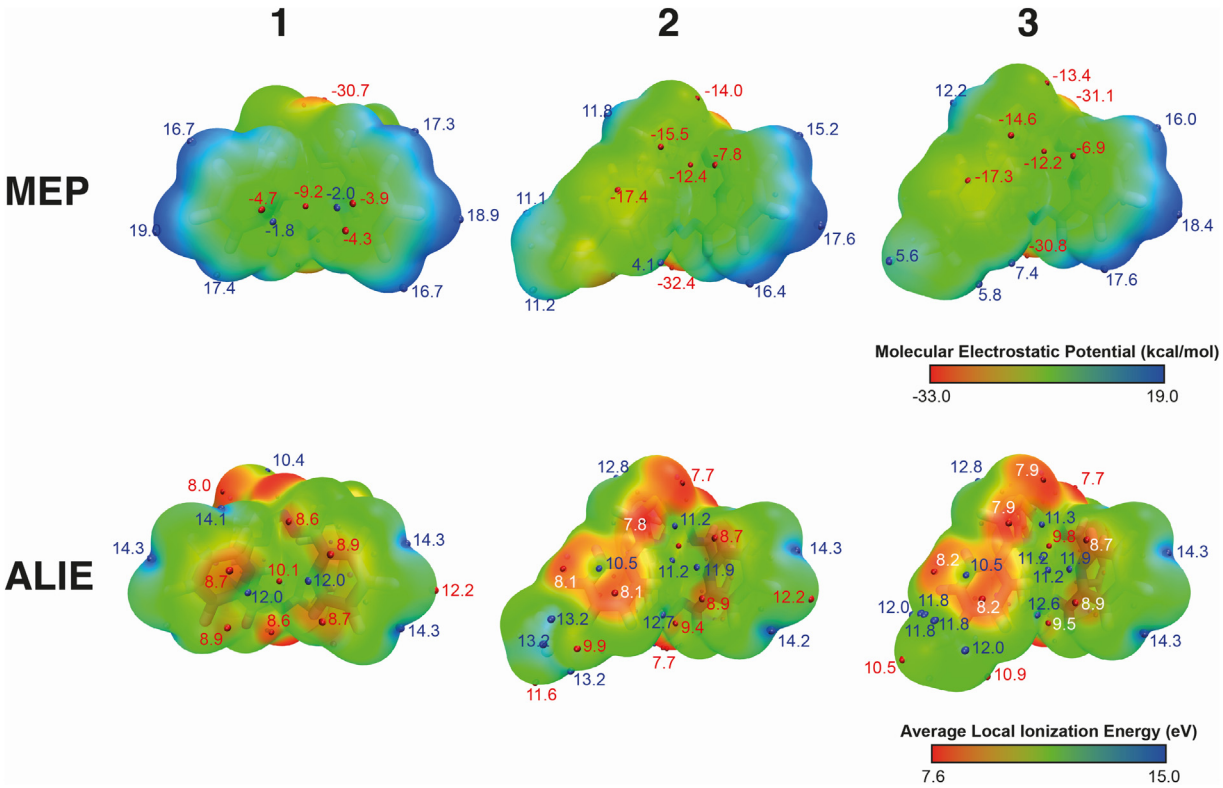

Fig. 4. MEP and ALIE are represented on the molecule surface of **1**–**3**. Red and blue points (at MEP labeled in kcal/mol and at ALIE labeled in eV) represent local minima and maxima, respectively.

are likely to be subjected to electrophilic attacks. In addition, Fukui indices are another type of quantum molecular descriptor considered relative indicators of molecule reactivity [27]. QTAIM analysis shows the electron density distribution, which is indicative of the bonding environment in the molecule. The potential changes caused by peripheral groups' presence reflect the weakening or strengthening of bonds [28].

The MEP maps (Fig. 4) show that the presence of $-OCH_3$, and $-CH_3$ groups at C13 in **2** and **3**, respectively, caused an increase in the electron density of the benzene ring, and decreased its local electrostatic potential from −4.7 kcal/mol to about −17 kcal/mol. On the other hand, introducing $-OCH_3$ and $-CH_3$ groups into the benzene ring lowers ALIE values (Fig. 4) from a local minimum and maximum of 8.7 and 12.0 eV for 1 to about 8 eV and 10.5 eV for **2** and **3**, respectively.

Since the substituents in **2** and **3** increase the electron density of the benzene ring, the energy required to ionize it decreases. However, there is relatively little difference in minimum and maximum values of MEP and ALIE between the three complexes (Fig. 4), indicating that the effects of substituents at C13 are localized to the substitution site and do not extend to a significant degree to the rest of the molecule. The minimum MEP values are in the range −31 to −32.5 kcal/mol, while maximum values are in the range 17.6 to 19.0 kcal/mol. These regions represent the most favorable sites for electrophilic and nucleophilic attacks. The most probable site for an electrophilic attack is the =*N*–N– moiety of each ligand, whereas the nucleophilic attacks tend to occur on C3-H of the pyridine ring. Maximum value of ALIE is 14.3 eV in all three complexes.

The Fukui functions for the electrophilic (f^-), radical (f^0) and nucleophilic (f^+) reactivities of all the complexes are shown in Figure S21 (Supplementary material). According to the results, neither $-OCH_3$ nor $-CH_3$ groups significantly impact the reactivity of the complexes. However, all the complexes seem more suitable for undergoing an electrophilic attack at the nitrogen atom of the =*N*–N– moiety that is not coordinated to Zn(II), compared to a radical or nucleophilic reaction. This result agrees with the fact that these ligands are protonated in that particular nitrogen atom when more acidic conditions are provided. In addition, these results agree with MEP and ALIE.

The QTAIM analysis was performed using structures obtained by the single-crystal XRD, showing electron density distribution and potential changes caused by the presence of peripheral groups. All three complexes share a similar pattern of interactions between the ligands and the Zn(II) ion (Figure S22, Supplementary material). Due to the negative charge on the nitrogen atom of each ligand, the interaction of the N2 with the Zn(II) represents the strongest type of interaction (b and e) among the ones between the ligands and the Zn(II) ion. Moreover, this type of interaction also has a significantly greater ionic nature (highest$\nabla^2\rho(r)$) due to the concentrated negative and positive charges on the ligand and Zn(II) ion, respectively. The substitution at C13 of the ligands' benzene ring does not significantly impact the interactions between the ligands and the Zn(II) ions (Figures S22 and S23, Table S10, Supplementary material). This agrees with the results of the local reactivity study, which showed only localized effects of the substitution.

3.6. Thermal analysis

The complexes were analyzed in air and argon by a simultaneous thermoanalytical technique, thermogravimetry-differential scanning calorimetry (TG-DSC). The compounds do not contain lattice or coordinated solvent molecules. Small mass loss (1.3%) observed on the TG curve of complex **1** from the onset temperature (137 °C) up to 200 °C is most probably a consequence of evaporation of the solvent (Fig. 5A), which overlaps with the beginning of thermal degradation of the compound **1**. Compounds **2** and **3**

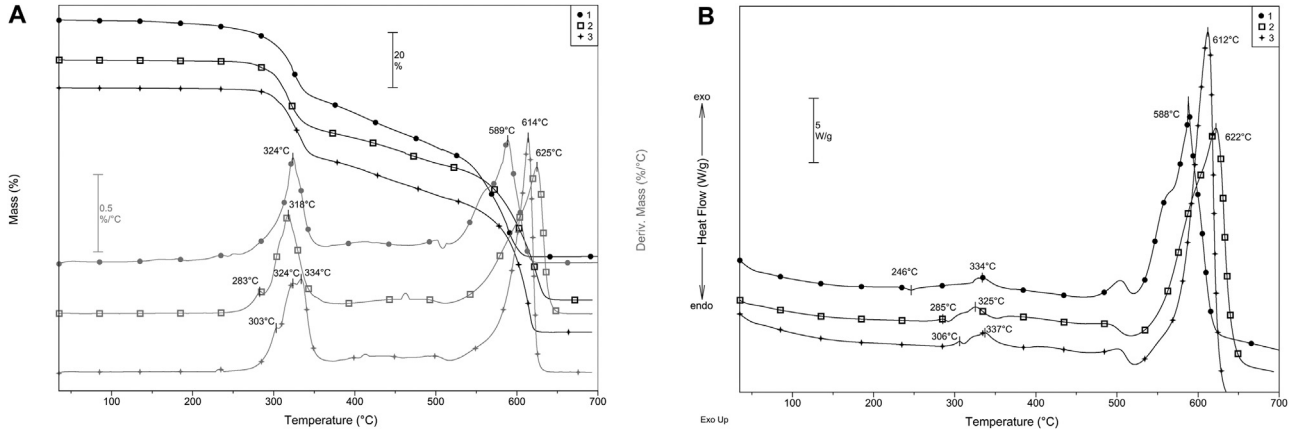

Fig. 5. (A) TG curves and corresponding derivative curves of **1**–**3** in the air; (B) DSC curves of **1**–**3** in the air.

lose only negligible mass (0.3 and 0.2%, respectively) in this temperature range. The decomposition of **2** begins at 254 °C. The first decomposition step with a DTG peak at 283 °C, with a mass loss of 2.9%, probably corresponds to the partial splitting of OCH_3 substituent from the phenyl ring of the ligand (4.54% mass). The following steps are more overlapped and can be separated neither in TG nor in DTG curves. The decomposition of **3** begins at 275 °C. The shape of TG and DTG curves for **2** and **3** indicates similar degradation mechanisms. The first DTG peak of **3** appears at 303 °C and it may be correlated to the release of the methyl group from the ligand that overlapped with the degradation and rearrangement of the thiazole-type ligand. Generally, the thermal decomposition of the complexes is the most intense around 300 °C with DTG maxima at 324, 318, and 334 °C for **1, 2**, and **3**, respectively. Above ~350 °C up to 500 °C, the decomposition processes of all complexes are slower, but continuous without stable intermediate formation. Above 500 °C there is a combustion of the organic part of the compounds. The corresponding DTG maxima are 589 (**1**), 625 (**2**), and 614 °C (**3**). The mass of the final remains of all compounds is constant above 700 °C and is probably ZnO, since the formation of other IR-active products can be excluded by IR spectra. The endothermic peak on the DSC curve of **1** at 246 °C (Fig. 5B) together with the TG curve suggests evaporation processes from 220 up to 260 °C. DSC curves for **2** and **3** show that these compounds do not change up to ~280 °C. The main decomposition step of both **2** and **3** at ~300 °C begins with a small exothermic peak before the main exothermic decomposition step due to oxidation processes. The combustion of the organic part of the complexes above 500 °C is also accompanied by exothermic peaks at 588, 622, and 612 °C for **1, 2**, and **3**, respectively.

The measurements were carried out in argon, too (Figure S24, Supplementary material). Up to ~400 °C, there is no significant difference between the decomposition of the complexes in an inert and an oxidative atmosphere. The endothermic peaks at 250–400 °C are more visible in argon. The main difference is that above 400 °C in the inert atmosphere the combustion of the compounds above 500 °C does not occur, therefore, the degradation is not complete up to 700 °C, while in the air the decomposition was complete with ZnO formation. In accordance, the DSC curves recorded in argon, do not show the transformation accompanied by heat effect in this temperature range.

3.7. Electrochemical studies

TH ligands have redox activity because of the electron transfer reaction of the hydrazone and thiazole moieties. Hydrazone groups of these ligands can undergo successive 2e⁻ based reduction and thiazole rings have an oxidation tendency with one-electron transfer reactions [29–32].

Table 2
Electrochemical parameters of the complexes.

	Peak Potentials[a] (V *vs* Ag/AgCl at 100 mVs^{-1} scan rate)			
Complexes	*R(1)*	*R(2)*	*R(3)*	*O(1)*
1	−1.63	−1.83	−2.23	0.65
2	−1.58	−1.79	−2.20	0.68
3	−1.62	−1.82	−2.22	0.64

[a] $E_{p,c}$ for reduction and $E_{p,a}$ for oxidation processes, which were derived from SWVs.

As shown in Figures S25-S27 (Supplementary material), all three complexes illustrate very similar SWVs and CVs responses in DMSO/TBAP media. Two successive 1e⁻ irreversible waves at around −1.50 (*R*(1)) and −1.80 V (*R*(2)) are recorded for the sequential reduction of each imine group to hydrazo products. At more negative potentials, the third reduction process occurs at about −2.0 V, for the further 2e⁻ reduction of two hydrazo groups of the complexes (at the same potential as the amine products). The different substituents on the ligands slightly alter the peak positions and do not influence the redox mechanism (Table 2). Complex **2** is the most easily reduced one. In addition to the reduction reactions, the complexes show a 2e⁻ oxidation process related to the oxidation of the two thiazole rings. CVs recorded with various vertex potentials (Figures S25B-S27B, Supplementary material) clearly indicate that the *R*(1) couples behave reversibly when the vertex potential is returned just after the first reduction wave. However, after the second and third reduction processes, all reductions become irreversible when the potential is changed. Moreover, small new waves are noticed during the reverse potential scans because of the possible chemical reactions that may occur after the second and third reduction processes.

Similar ligands with thiazole moieties have a tendency to undergo 1e⁻ oxidation process [33–35]. For instance, Özkütük et al. reported the irreversible oxidation wave of six different thiazole ligands at around 1.0 V *vs* Ag/AgCl in DMSO/TBATFB electrolyte [33]. The studies indicate that the redox mechanisms of similar ligands could be easily modified with substitution and upon coordination [36–39]. Herein, the voltammetric results suggest that coordination of the TH ligands does not influence the redox responses of the ligands due to the redox inactivity of Zn(II). Controlled potential electrolysis (CPE) was performed to ascertain the number of transferred electrons throughout each redox wave. The CPE analysis indicates that 1, 1, and 2 electrons were transferred during the *R*(1), *R*(2), and *R*(3) processes, respectively. Similarly, *O*(1) is found

$$[L-Zn^{2+}-L] - 2e^- \underset{}{\overset{O(1)}{\rightleftharpoons}} [L^{1+}-Zn^{2+}-L^{1+}]$$

$$[L-Zn^{2+}-L] + 1e^- \overset{R(1)}{\rightleftharpoons} [L^{1-}-Zn^{2+}-L]$$

$$[L^{1-}-Zn^{2+}-L] \xrightarrow{\text{succeeding chemical reaction}} \textit{Unknown products}$$

$$[L^{1-}-Zn^{2+}-L] + 1e^- \overset{R(2)}{\rightleftharpoons} [L^{1-}-Zn^{2+}-L^{1-}]$$

$$[L^{1-}-Zn^{2+}-L^{1-}] \xrightarrow{\text{succeeding chemical reaction}} \textit{Unknown products}$$

$$[L^{1-}-Zn^{2+}-L^{1-}] + 2e^- \overset{R(3)}{\rightleftharpoons} [L^{2-}-Zn^{2+}-L^{2-}]$$

Scheme 1. Redox mechanism of the complexes in DMSO/TBAP electrolyte.

to be a $2e^-$ transfer process. The reduction and oxidation mechanisms of the complexes are presented in Scheme 1.

In situ UV–Vis spectroelectrochemical analysis was performed to determine the color and spectra of the reduced and oxidized species and to support the proposed mechanisms derived from the voltammetric analysis. Three complexes showed very similar *in situ* UV–Vis spectroelectrochemical responses. As an example, the response of **1** is presented in Fig. 5.

Neutral complex **1** shows distinct intraligand (n $\rightarrow$ π^* and $\pi \rightarrow \pi^*$) transition bands at 266, 297, 338, 440, 468, and 498 nm. During the *R*(1) process at an applied constant potential of –1.70 V, the bands at 338 and 498 nm decrease in absorbance intensity, while all other bands remain unchanged. Moreover, two new charge transfer bands are observed at 355 and 392 nm (Fig. 6A). Well-resolved isosbestic points at 321, 347, and 493 nm indicate the chemical reversibility of the reduced species. Comparison of the spectral changes observed during the *R*(1) with those assigned to the central metal reduction of a similar complex [40], suggests that *R*(1) process can be assigned to the ligand electron transfer process. All bands increase in intensity during the *R*(2) (at –1.95 V) as illustrated in Fig. 6B. None of the isosbestic points was not recorded due to the instability of the dianionic species. During the *R*(3) reaction, all bands decreased in intensity due to the complex's fragmentation after forming the amine products. At the applied potential of 1.0 V (*O*(1)), while the intensity of the bands at 440, 468, and 498 nm were reduced, the intensity of the bands at 266, 297, and 338 nm was increased. Moreover, two new bands are observed at 393 and 592 nm (Fig. 6C). The isosbestic points at 418 and 523 nm point to the chemical reversibility of the oxidation reaction of the complex. These spectral changes agree with the spectroelectrochemical responses of thiazolyl-containing ligands [12,41]. As illustrated in the chromaticity diagram (Fig. 6D), the orange color (point□; $x = 0.489$ and $y = 0.422$) of the complex becomes light orange (point ○; $x = 0.457$ and $y = 0.430$), then yellow (point △; $x = 0.457$ and $y = 0.430$) and colorless (point ▼; $x = 0.457$ and $y = 0.430$) after the reduction reactions. Similarly, a red color (point ☆; $x = 0.457$ and $y = 0.430$) is observed after the oxidation of the complex.

3.8. Photophysical and computational study

Complexes **1**–**3** exhibit solid-state luminescence at RT and at 77 K after irradiation with UV light (Fig. 7A). Thus, at RT, **1**–**3** display an emission at 625 ($\Phi = 3.7\%$), 610 ($\Phi = 2.8\%$), and 633 nm ($\Phi = 3.7\%$), respectively with lifetimes of 450 (**1**), 433 (**2**) and 393 ns (**3**). These lifetimes in the nanosecond range, together with the small stokes shift and the fact that the excitation spectra are included in the absorption ones, (see Figures S28–S30, Supplementary material) point out that fluorescent processes cause the observed luminescent emissions. At 77 K, the new emissions display two maxima located at 586 and 613 (**1**), 580 and 613 (**2**), and 594, 614 nm (**3**), and shoulders at lower energy, perhaps arising from a vibronic structure. These structured profiles are likely to be related to vibronic structures since the difference in energy between adjacent peaks appears around 750 cm^{-1}. This energy range would correspond to C–S stretching vibrations. Accordingly, we can propose that the ligands are involved in the luminescent emissions (*vide infra*).

Obtained results are corroborated by the analysis of the molecular orbitals and the computed singlet-singlet electronic excitations calculated by DFT and TD-DFT, respectively. As a representative example of this set of complexes, a theoretical model system **1**a was used. This model system is completely DFT-B3LYP optimized and built up based on the crystal structure obtained from the single-crystals XRD studies for **1**. The computation of the electronic structure of the frontier molecular orbitals reveals that these show a ligand-based composition (Fig. 7B). The first 50 singlet-singlet excitations at the TD-DFT level for model system **1**a were computed and compared with the experimental excitation and absorption spectra of **1** (Figure S32, Supplementary material). We analyzed the most intense singlet-singlet transitions (Table S11 and Figures S33 and S34, Supplementary material). Ligand-to-ligand charge transfer (LLCT) and intra-ligand (IL) appear to be allowed electronic excitations. The origin of the emissive properties of **1**–**3** can be described by the singlet-singlet transitions displaying higher oscillator strengths since the lifetime is in the nanosecond range. Therefore, an admixture of 1LLCT and 1IL electronic transitions is responsible for the appearance of the emission of investigated compounds. Some of us recently reported a similar assignment on related octahedral Zn(II) complexes [14].

A deeper analysis of the MOs (Figures S33 and S34, Supplementary material) shows that lower energy singlet-singlet transitions arise mainly from orbitals HOMO and HOMO-1 and arrive to orbitals LUMO and LUMO+1. In contrast, higher energy singlet-singlet transitions arise from a different part of the same ligands in orbitals HOMO-3, HOMO-4 and HOMO-9 and arrive again to LUMO and LUMO+1 (see Figures S33 and S34, Supplementary material). In all cases, the C–S bonds are involved in all the MOs, supporting the previous assignment of the experimentally observed emissions.

3.9. Anticancer activity

3.9.1. Antiproliferative activity

Due to non-electrolyte nature, the complexes are soluble only in DMSO. The anticancer potential of investigated compounds was initiated by determining their solubility and stability in the culture medium containing 0.25% v/v DMSO. Among all synthesized compounds, only **1** is soluble in the culture medium containing 0.25% v/v DMSO and therefore it was further studied in that respect. The buffered aqueous solution behavior of **1** with respect to hydrolysis was studied by UV/vis spectroscopy over 48 h under conditions similar to those used in the antiproliferative activity determination experiment (PBS solution of **1** containing 0.25% v/v DMSO at 298 K). Complex **1** showed only a 12% decrease of the intensity of the band with an absorption maximum at 465.4 nm after 48 h (Figure S40, Supplementary material).

The antiproliferative activity of **1** has been examined at the following solid tumor cell lines: WiDr (colon), HBL-100 (breast), T-47D (breast), HeLa (cervix), and A549 (non-small cell lung) and expressed as GI_{50} values. Obtained GI_{50} values for **1** as well as GI_{50} values previously determined for corresponding ligand (HLS^1) [1] and anticancer drugs cisplatin and 5-fluorouracil (5-FU) are presented in Table 3. The obtained results indicated that 1 exhibited appreciable activity on all six investigated cell lines, with GI50 values lower than 2 μM. **1** appeared to be more active than the

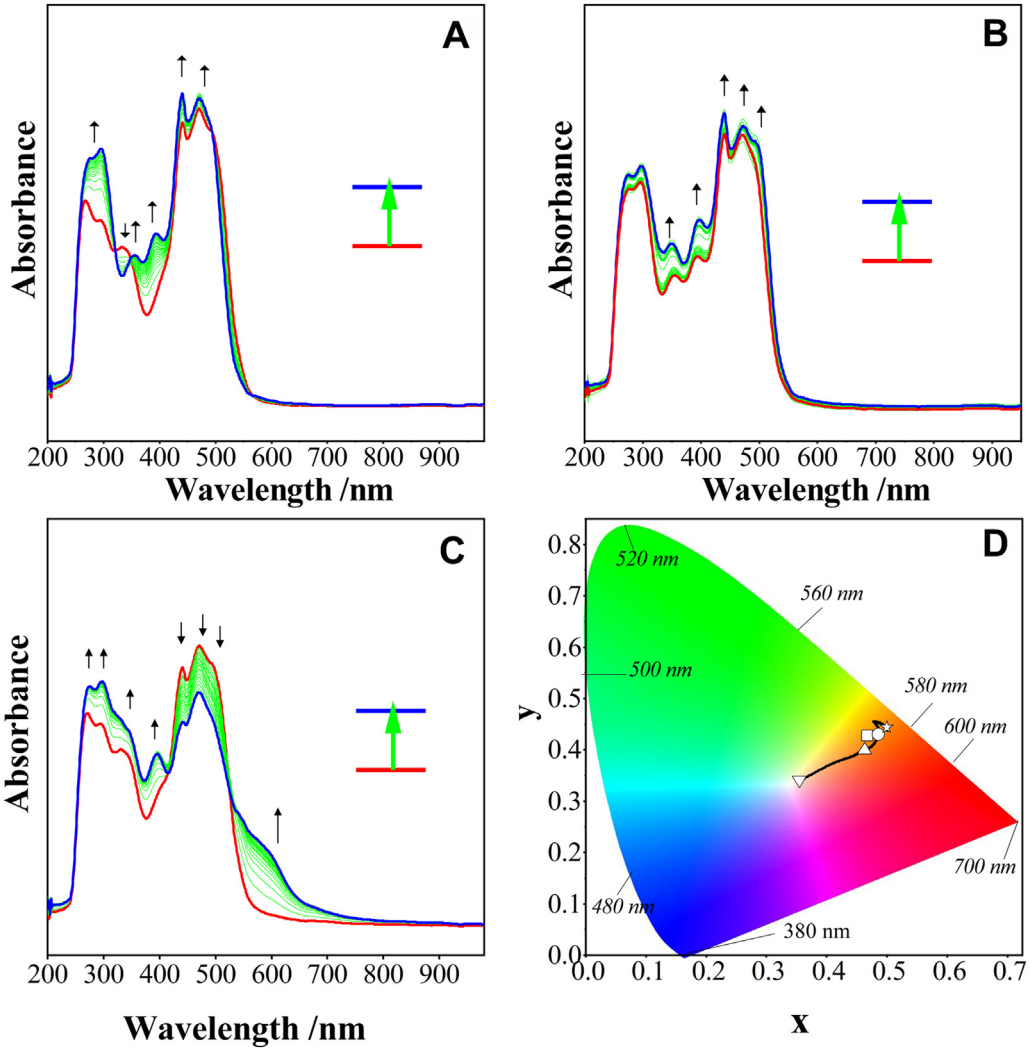

Fig. 6. In situ UV–Vis spectroelectrochemical results for **1** (arrows illustrate the change of the spectra under applied potentials): A) E_{app} = −1.75 V, B) E_{app} = −1.95 V, and C) E_{app} = 1.00 V in TBAP/DMSO media; D) color of the neutral, reduced, and oxidized complex (Neutral: □; *R*(1): ○; R(2): △; R(3): ▼; O(1): ☆).

Table 3
Antiproliferative activity (GI_{50}) of the investigated compounds.

	GI_{50} (μM)				
Compound	A549	HBL-100	HeLa	T-47D	WiDr
HLS^1 *	3.0 ± 1.1	5.8 ± 1.7	5.2 ± 1.1	22 ± 0.92	n.a.**
1	1.4 ± 0.23	1.2 ± 0.14	1.0 ± 0.06	1.4 ± 0.25	1.6 ± 0.42
Cisplatin	1.9 ± 0.2	2.0 ± 0.3	15 ± 2.3	4.9 ± 0.2	1.9 ± 0.2
5-FU	2.2 ± 0.3	4.4 ± 0.7	16 ± 4.5	43 ± 16	49 ± 6.7

* Literature data [1]. **n.a. - not active (GI_{50} > 100 µM).

corresponding ligand, and cisplatin and 5-FU as the reference compounds.

3.9.2. Analyses of cell cycle phases and progression

Uncontrolled cell division is one of the hallmarks of cancer [42]. Therefore, the activity of many chemotherapeutics agents relies on modulating cell cycle phases [43]. To establish whether HLS^1 and **1** influence cell cycle progression, the distribution of A549-treated cells in different cell cycle stages was determined using flow cytometry. As shown in Fig. 8, both compounds induced concentration-dependent accumulation cells in G_0/G_1 phase, with a concomitantly decreased number of cells in the S-phase; however, no changes were observed in the G_2/M phase. The G_0/G_1 fraction was ∼30% in DMSO-treated control cells and increased up to 52.9 ± 1.1%, and 48.5 ± 3.5%, with 20 μM of HLS^1 and **1**, respectively. This suggested that both compounds might inhibit cell proliferation by inducing cell G_0/G_1 arrest.

3.9.3. Evaluation of pro-apoptotic properties

To further understand the mechanism underlying the cytotoxicity of HLS^1 and **1** on A549 cells, their pro-apoptotic properties were investigated using flow cytometry. Cells were subjected to increasing doses of both compounds for 48 h and stained with Annexin V-FITC and 7-AAD. This combination allows the differentia-

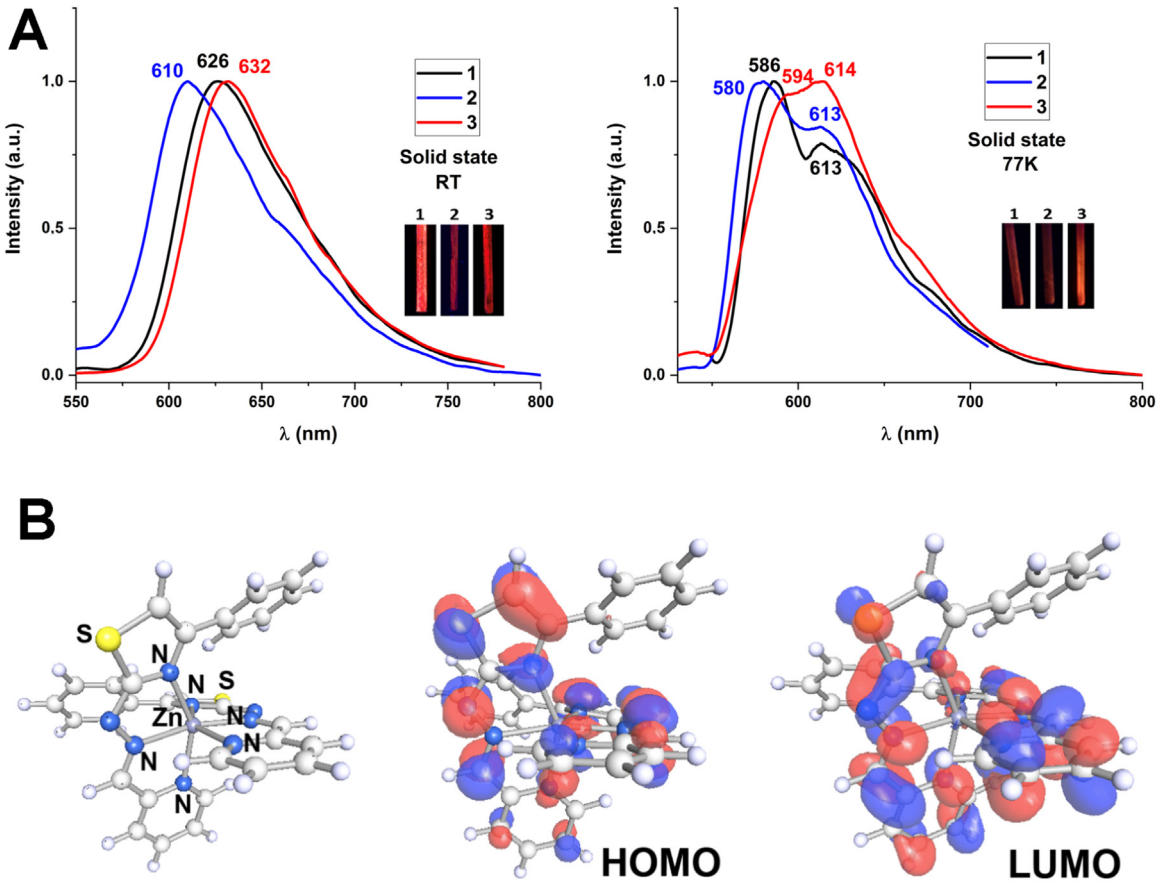

Fig. 7. (A) Solid state emission spectra for **1**–**3** at RT (left) and at 77 K (right). (B) Theoretical model system **1**a (left) and HOMO (middle) and LUMO (right) obtained at the DFT theory level.

tion among necrotic cells (Annexin V-FITC(-)/7-AAD(+)), late-phase apoptotic cells (Annexin V-FITC(+)/7-AAD(+)), early phase apoptotic cells (Annexin V-FITC(+)/7-AAD(−)), and viable cells (Annexin V-FITC(-)/7-AAD(−)). Physical changes in the plasma membrane such as the exposition of the negatively charged phosphatidylserine in the outer leaflet of the membrane, are one of the events occurring in apoptotic cell death [44]. Moreover, during the late apoptotic and necrotic phases the integrity of the plasma membrane is compromised [45]. As depicted in Figure S41 (Supplementary material), HLS[1] slightly increased the populations of both apoptotic positive cells (early + late) independently of its concentration. Treatment of A549 cells with **1** led to a concentration-dependent increase in apoptotic cells. This effect was strongly enhanced in comparison to the ligand alone. The most notable increase in the number of late apoptotic cell death was noticed for 15 and 20 μM of **1**, where the population raised to 48.2 ± 1.85% and 62.5 ± 4.5%, respectively. The highest concentrations of **1** increased the necrotic fraction of cells, but significantly only after treatment with 20 μM ($p < 0.01$). In addition, it is worth noting that Etoposide's fraction of apoptotic cells (early and late) was only 37.4 ± 4.8%. Typical cytomorphological features of apoptosis, like chromatin condensation, cell shrinkage, cell blebbing, and apoptotic bodies were also observed by fluorescent microscopy after A549 cells were treated with HLS[1] and **1** (Figure S42, Supplementary material).

3.9.4. Evaluation of caspase-3 and −7 activity

Throughout apoptosis, executioner caspases-3 and −7 are cleaved and activated, leading to catalysing proteolysis of many key cellular proteins [46]. To investigate whether HLS[1] and **1** induce caspase-dependent apoptosis, cells were subjected to several concentrations of the compounds and analyzed by flow cytometry. Figure S43 (Supplementary material) depicts representative dot-plots and quantitative analyses. A concentration-dependent activation of caspase-3/7 was noticed for both compounds after 48 h of treatment. In addition, compounds exhibited similar activity in all tested conditions, leading to approximately threefold augmentation in caspase-3/7 expression compared to the vehicle.

3.9.5. Evaluation of calcium efflux

Deregulation of calcium (Ca^{2+}) homeostasis is a hallmark of cancer cells. Alteration of intracellular concentration of Ca^{2+} is observed in metastasis and apoptosis resistance [47,48]. In the majority of cells, a key role in Ca^{2+} storage has the endoplasmic reticulum (ER) [49]. During stress, ER leads to efflux Ca^{2+} from its lumen inducing accumulation in the mitochondrial matrix. Mitochondrial outer membrane permeabilization and cytochrome c release are signs of proapoptotic mitochondrial alteration. They are both triggered by the influx of Ca^{2+} into mitochondria [50]. Intracellular levels of Ca^{2+}were measured in A549 cells, after treatment with HLS[1] and **1** at increasing doses for 24 h. Figure S44 (Supplementary material) shows that both compounds induce potent, time-dependent increases in free Ca^{2+} levels. Importantly, after the complexation of the HLS[1] compound, Ca^{2+} efflux from the ER was significantly higher than this caused by ligand alone. Additionally, it is worth emphasizing that A549 cells treated with **1** at 20 μM led to a massive accumulation of cytosolic Ca^{2+}, which was revealed as a 93±1.32% increase compared to the vehicle. These results indicated that HLS[1] and **1** could dose-dependently induce ER-mediated apoptotic death in A549 cells.

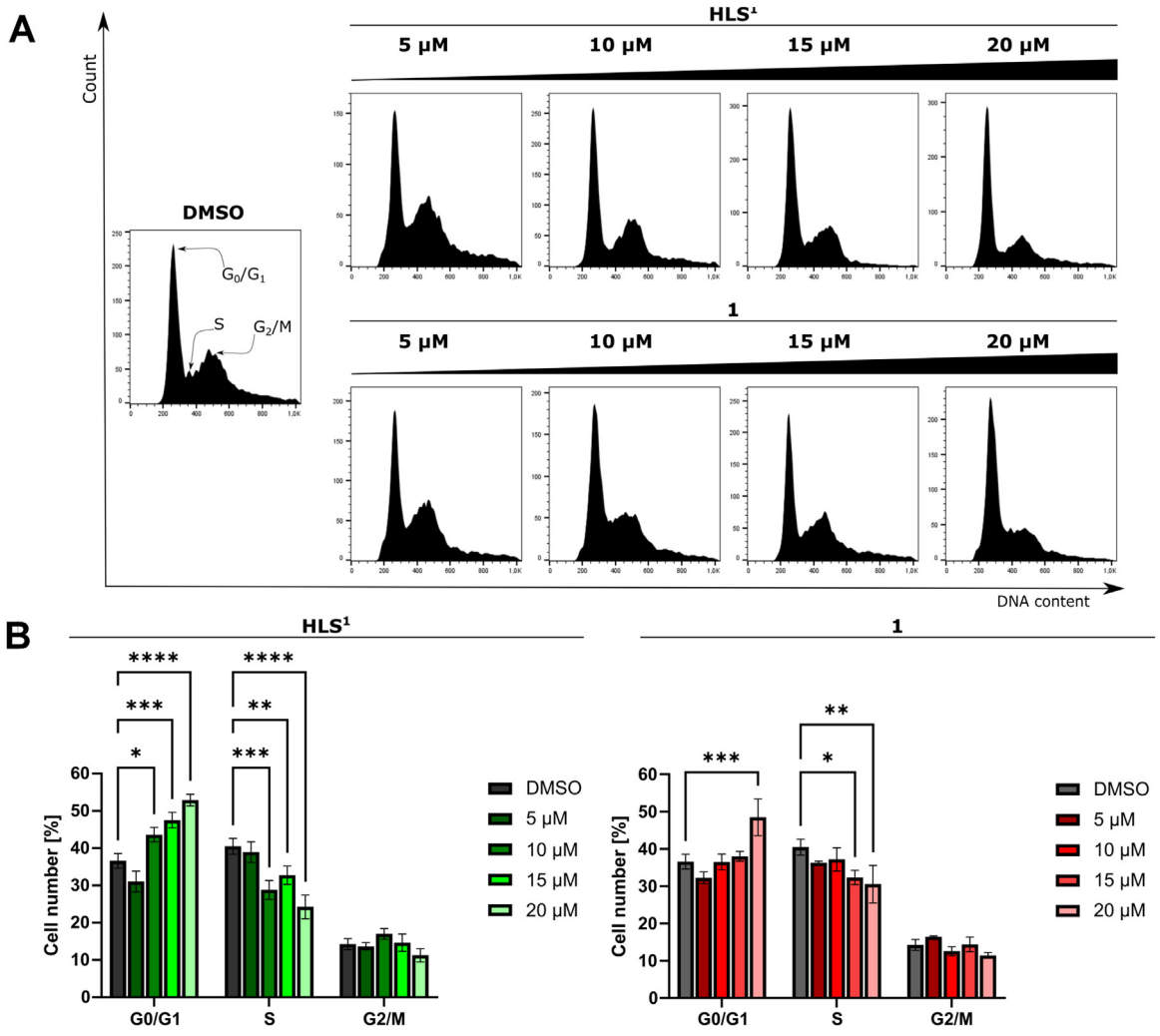

Fig. 8. Cell cycle distribution analysis in A549 cells after 48 h of treatment with HLS^1 and **1**. DMSO was used as a benchmark compound. (A) Illustrative histograms; (B) Graph bar representation of the quantification of the analysis. Error bars reflect the SEM of data from three independent experiments. Statistical differences were tested with a one-way ANOVA test.
* $p < 0.01$, ** $p < 0.001$, *** $p < 0.0001$, **** $p < 0.00001$ in comparison to DMSO.

3.9.6. Genotoxic properties

Cell cycle arrest and apoptosis can be triggered by specific DNA lesions [51]. In terms of cell death, double-strand breaks (DSB) are considered as deadliest. One of the early steps in response to DSB is the phosphorylation of H2AX at Ser 139 at the site of DNA damage [52]. The DNA-damaging effects of HLS^1 and **1** were assessed after the treatment of A549 cells with various concentrations of the compounds by flow cytometry. As shown in Figure S45 (Supplementary material), both compounds induce a significant, concentration-dependent increase of DSBs compared to DMSO-treated cells after 48 h. In the concentration range of 5 - 15 μM, **1** exhibited stronger genotoxic properties than HLS^1; however, at 20 μM both compounds exerted similar activity, leading to 55.4 ± 1.6% ($p < 0.0001$), and 61.4 ± 2.5% ($p < 0.00001$) increase of γH2AX positive cells for HLS^1, and **1**, respectively.

4. Conclusions

In this work, the synthesis and characterization of Zn(II) complexes **1**–**3** with deprotonated forms of 1,3-TH ligands HLS^{1-3} was presented. Single-crystal XRD analysis reveals that deprotonated forms of HLS^{1-3} behave as NNN tridentates upon coordination to Zn(II), as it was noticed for their neutral forms. All compounds were shown to be relatively thermally stable, with decomposition starting in the 220–250 °C temperature range. Since the only structural difference between investigated compounds is the presence of additional groups at C13 of the benzene ring, it was possible to evaluate the impact of additional –Me and –OMe groups on selected molecular descriptors. The differences between maximum and minimal values of MEP and ALIE between all three complexes are low, suggesting that substituent influence is localized to the substitution site. All these parameters indicate that the non-coordinated nitrogen atom of the hydrazone moiety is the most favorable for electrophilic attacks, while the pyridine hydrogen atom in the anti-position concerning the nitrogen atom is the most favorable for nucleophilic attacks. The reactivity to an electrophilic attack to =*N*–N functional group is preferred over radical or nucleophilic reaction. Finally, QTAIM calculations indicate the significant ionic nature of all Zn–N bonds. All Zn complexes have similar imine-based-reduction and thiazole-based oxidation reactions. The substituents on the ligands did not considerably influence their redox responses. Predominant spectral changes were observed during the first reduction and oxidation processes that caused distinct spectral color changes indicating their possible functionality for electrochromic applications.

The obtained results regarding the photophysical properties of novel asymmetrical complexes **1–3** herein agree with our previous hypothesis [14] since all three investigated complexes are asymmetric and show luminescent properties. Comparison of emission wavelengths of **1–3** with the corresponding Zn(II) complexes with the neutral form of the ligands shows that the emissions of **1–3** are shifted to lower energy and originate from an admixture of ^{1}IL and ^{1}LLCT electronic transitions. This suggests that the deprotonation of the ligands mainly affects the relative energies of electronic levels in the complexes, resulting in similar photoluminescence mechanisms and quantum yields with a small shift in emission energy.

Since only **1** was soluble in the culture medium containing 0.25 v/v DMSO, it was the only compound tested for the antiproliferative activity on selected cancer cell lines. GI_{50} values of **1** were below 2 μM. Flow cytometry studies confirmed that the antiproliferative action results from blocking the G1/S phase in A549 cells. Additionally, the compound induced pronounced DNA damage as well as distinctive morphological and biochemical changes associated with apoptosis features, such as chromatin condensation, exposure of phosphatidylserine and activation of caspases. Further analysis revealed that **1** significantly altered calcium homeostasis, indicating ER stress-mediated apoptotic death in A549 cells. It is worth emphasizing that **1** showed markedly increased anticancer activity than the corresponding ligand. Obtained results indicate the potential application of Zn(II) complexes with 1,3-THs in cancer therapy.

Declaration of Competing Interest

The authors declare that they have no known competing financial interests or personal relationships that could have appeared to influence the work reported in this paper.

CRediT authorship contribution statement

Jovana B. Araškov: Investigation, Writing – original draft. **Natalia Maciejewska:** Investigation, Writing – original draft. **Mateusz Olszewski:** Investigation, Writing – original draft. **Aleksandar Višnjevac:** Investigation, Resources. **Vladimir Blagojević:** Formal analysis, Supervision. **Henrique S. Fernandes:** Investigation. **Sérgio F. Sousa:** Formal analysis, Resources, Supervision, Validation. **Adrián Puerta:** Investigation. **José M. Padrón:** Investigation, Resources. **Berta Barta Holló:** Investigation, Visualization, Writing – original draft. **Miguel Monge:** Investigation, Visualization. **María Rodríguez-Castillo:** Investigation, Visualization. **José M. López-de-Luzuriaga:** Formal analysis, Resources, Supervision, Validation, Writing – original draft. **Özlem Uğuz:** Investigation, Writing – original draft. **Atıf Koca:** Resources, Supervision, Validation, Writing – original draft. **Tamara R. Todorović:** Resources, Supervision, Visualization, Writing – original draft, Writing – review & editing. **Nenad R. Filipović:** Conceptualization, Supervision, Writing – original draft, Writing – review & editing.

Data availability

Data will be made available on request.

Acknowledgments

The authors acknowledge the financial support of the Ministry of Education, Science and Technological Development of the Republic of Serbia (Contract No's. 451–03–68/2022–14/200116, 451–03–68/2022–14/200125, 451-03-47/2023-01/200116 and 451–03–68/2022–14/200168). A.P. and J.M.P. thank the Canary Islands Government (ProID2020010101, ACIISI/FEDER, UE) for financial support. AP thanks the EU Social Fund (FSE) and the Canary Islands ACIISI for a predoctoral grant TESIS2020010055. J.M.L.L Grant PID2019–104379RB-C22 funded by MCIN/AEI/10.13039/501100011033 and by "ERDF A way of making Europe" is acknowledged. S.F.S thanks the national funds from the Portuguese Foundation for Science and Technology (FCT) under the scope of the strategic funding UIDP/04378/2020 and UIDB/04378/2020. S.F.S. acknowledges FCT by funding 2020.01423.CEECIND/CP1596/CT0003. Some of the calculations were produced with the support of the INCD funded by the FCT and FEDER under project 01/SAICT/2016 number 022153, and projects CPCA/A00/7140/2020 and CPCA/A00/7145/2020. A.K. and Ö.U. acknowledge the financial support of the Academy of Sciences (TÜBA) for the financial support.

Supplementary materials

Supplementary material associated with this article can be found, in the online version, at doi:10.1016/j.molstruc.2023.135157.

References

[1] J.B. Araškov, M. Nikolić, S. Armaković, S. Armaković, M. Rodić, A. Višnjevac, J.M. Padrón, T.R. Todorović, N.R. Filipović, Structural, antioxidant, antiproliferative and in–silico study of pyridine-based hydrazonyl–selenazoles and their sulphur isosteres, J. Mol. Struct. 1240 (2021) 130512, doi:10.1016/j.molstruc.2021.130512.

[2] M. Haroon, M. Khalid, K. Shahzadi, T. Akhtar, S. Saba, J. Rafique, S. Ali, M. Irfan, M.M. Alam, M. Imran, Alkyl 2-(2-(arylidene)alkylhydrazinyl)thiazole-4-carboxylates: synthesis, acetyl cholinesterase inhibition and docking studies, J. Mol. Struct. 1245 (2021) 131063, doi:10.1016/j.molstruc.2021.131063.

[3] P.A. Channar, A. Saeed, S. Afzal, D. Hussain, M. Kalesse, S.A. Shehzadi, J. Iqbal, Hydrazine clubbed 1,3-thiazoles as potent urease inhibitors: design, synthesis and molecular docking studies, Mol. Divers. 25 (2021) 787–799, doi:10.1007/s11030-020-10057-7.

[4] A.M. El-Naggar, M.A. El-Hashash, E.B. Elkaeed, Eco-friendly sequential one-pot synthesis, molecular docking, and anticancer evaluation of arylidene-hydrazinyl-thiazole derivatives as CDK2 inhibitors, Bioorg. Chem. 108 (2021) 104615, doi:10.1016/j.bioorg.2020.104615.

[5] A.M. Srour, N.S. Ahmed, S.S. Abd El-Karim, M.M. Anwar, S.M. El-Hallouty, Design, synthesis, biological evaluation, QSAR analysis and molecular modelling of new thiazol-benzimidazoles as EGFR inhibitors, Bioorganic Med. Chem. 28 (2020) 115657, doi:10.1016/j.bmc.2020.115657.

[6] B. Sever, M.D. Altıntop, Y. Demir, G. Akalın Çiftçi, Ş. Beydemir, A. Özdemir, Design, synthesis, *in vitro* and in silico investigation of aldose reductase inhibitory effects of new thiazole-based compounds, Bioorg. Chem. 102 (2020) 104110, doi:10.1016/j.bioorg.2020.104110.

[7] N.P. Veeranna, Y.D. Bodke, M. Basavaraju, K.M.M. Pasha, Synthesis of some novel isatin-thiazole conjugates and their computational and biological studies, Struct. Chem. 33 (2022) 897–906, doi:10.1007/s11224-022-01892-5.

[8] L.H.B. Maganti, D. Ramesh, B.G. Vijayakumar, M.I.K. Khan, A. Dhayalan, J. Kamalraja, T. Kannan, Acetylene containing 2-(2-hydrazinyl)thiazole derivatives: design, synthesis, and *in vitro* and in silico evaluation of antimycobacterial activity against Mycobacterium tuberculosis, RSC Adv 12 (2022) 8771–8782, doi:10.1039/d2ra00928e.

[9] S.K. Bharti, S.K. Patel, G. Nath, R. Tilak, S.K. Singh, Synthesis, characterization, DNA cleavage and *in vitro* antimicrobial activities of copper(II) complexes of Schiff bases containing a 2,4-disubstituted thiazole, Transit. Met. Chem. 35 (2010) 917–925, doi:10.1007/s11243-010-9412-8.

[10] P. Bera, A. Aher, P. Brandao, S.K. Manna, I. Bhattacharyya, G. Mondal, A. Jana, A. Santra, P. Bera, Anticancer activity, DNA binding and docking study of M(II)-complexes (M = Zn, Cu and Ni) derived from a new pyrazine–thiazole ligand: synthesis, structure and DFT, New J. Chem. 45 (2021) 11999–12015, doi:10.1039/d0nj05883a.

[11] H. Elshaflu, S. Bjelogrlić, C.D. Muller, T.R. Todorović, M. Rodić, A. Marinković, N.R. Filipović, Co(III) complex with (E)-2-(2-(pyridine-2-ylmethylene)hydrazinyl)-4-(4-tolyl)-1,3-thiazole: structure and activity against 2-D and 3-D cancer cell models, J. Coord. Chem. 69 (2016) 3354–3366, doi:10.1080/00958972.2016.1232404.

[12] N.R. Filipović, H. Elshaflu, S. Grubišić, L.S. Jovanović, M. Rodić, I. Novaković, A. Malešević, I.S. Djordjević, H. Li, N. Šojić, A. Marinković, T.R. Todorović, Co(III) complexes of (1,3-selenazol-2-yl)hydrazones and their sulphur analogues, Dalt. Trans. 46 (2017) 2910–2924, doi:10.1039/c6dt04785h.

[13] S.B. Marković, N. Maciejewska, M. Olszewski, A. Višnjevac, A. Puerta, J.M. Padrón, I. Novaković, S. Kojić, H.S. Fernandes, S.F. Sousa, S. Ramotowska, A. Chylewska, M. Makowski, T.R. Todorović, N.R. Filipović, Study of the anticancer potential of Cd complexes of selenazoyl-hydrazones and their sulfur isosters, Eur. J. Med. Chem. (2022) 238, doi:10.1016/j.ejmech.2022.114449.

[14] J. Araškov, A. Višnjevac, J. Popović, V. Blagojević, H.S. Fernandes, S. Sousa, I. Novakovic, J.M.M. Padrón, B. Hollo, M. Monge, M. Rodriguez-Castillo, J.M. López-de-Luzuriaga, N.R. Filipović, T.R. Todorović, Zn(II) complexes with thiazolyl-hydrazones: structure, intermolecular interactions, photophysical properties,

computational study and anticancer activity, CrystEngComm 24 (2022) 5194, doi:10.1039/d2ce00443g.
[15] A. Borges, M. Simões, T.R. Todorović, N.R. Filipović, A.T. Garcia-Sosa, Cobalt complex with thiazole-based ligand as new pseudomonas aeruginosa quorum quencher, biofilm inhibitor and virulence attenuator, Molecules 23 (2018) 1385, doi:10.3390/molecules23061385.
[16] M. Pellei, F. Del Bello, M. Porchia, C. Santini, Zinc coordination complexes as anticancer agents, Coord. Chem. Rev. 445 (2021) 214088, doi:10.1016/j.ccr.2021.214088.
[17] M. Porchia, M. Pellei, F. Del Bello, C. Santini, Zinc complexes with nitrogen donor ligands as anticancer agents, Molecules 25 (2020) 5814, doi:10.3390/molecules25245814.
[18] X.Z. Zou, A.S. Feng, Y.Z. Liao, X.Y. Xu, H.Y. Wen, A. You, M. Mei, Y. Li, Pyridine hydrazyl thiazole metal complexes: synthesis, crystal structure, antibacterial and antitumor activity, Inorg. Chem. Commun. 118 (2020) 1–5, doi:10.1016/j.inoche.2020.108030.
[19] Z. Xun-Zhong, F. An-Sheng, Z. Fu-Ran, L. Min-Cheng, L. Yan-Zhi, M. Meng, L. Yu, Synthesis, crystal structures, and antimicrobial and antitumor studies of two zinc(II) complexes with pyridine thiazole derivatives, Bioinorg. Chem. Appl. 2020 (2020) 1–9, doi:10.1155/2020/8852470.
[20] X. Zou, P. Shi, A. Feng, M. Mei, Y. Li, Two metal complex derivatives of pyridine thiazole ligand: synthesis, characterization and biological activity, Transit. Met. Chem. 46 (2021) 263–272, doi:10.1007/s11243-020-00442-4.
[21] X. Zou, Y. Liao, C. Yang, A. Feng, X. Xu, H. Jiang, Y. Li, Synthesis, X-ray structures, and biological activity of Zn(II) and cd(II) complexes with pyridine thiazolone derivatives, J. Coord. Chem. 74 (2021) 1009–1027, doi:10.1080/00958972.2020.1869952.
[22] F. Dumur, Zinc complexes in OLEDs: an overview, Synth. Met. 195 (2014) 241–251, doi:10.1016/j.synthmet.2014.06.018.
[23] H. Xu, R. Chen, Q. Sun, W. Lai, Q. Su, W. Huang, X. Liu, Recent progress in metal-organic complexes for optoelectronic applications, Chem. Soc. Rev. 43 (2014) 3259–3302, doi:10.1039/c3cs60449g.
[24] J.J. McKinnon, D. Jayatilaka, M.A. Spackman, Towards quantitative analysis of intermolecular interactions with Hirshfeld surfaces, Chem. Commun. 37 (2007) 3814–3816, doi:10.1039/B704980C.
[25] M.A. Spackman, J.J. McKinnon, Fingerprinting intermolecular interactions in molecular crystals, CrystEngComm 4 (2002) 378–392, doi:10.1039/b203191b.
[26] T. Maity, H. Mandal, A. Bauzá, B.C. Samanta, A. Frontera, S.K. Seth, Quantifying conventional C-H···π(aryl) and unconventional C-H···π(chelate) interactions in dinuclear Cu(II) complexes: experimental observations, Hirshfeld surface and theoretical DFT study, New J. Chem. 42 (2018) 10202–10213, doi:10.1039/c8nj00747k.
[27] O.R. Klisurić, S.J. Armaković, S. Armaković, S. Marković, T.R. Todorović, G. Portalone, K. Novović, J. Lozo, N.R. Filipović, Structural, biological and in-silico study of quinoline-baed chalcogensemicarbazones, J. Mol. Struct. 1203 (2020) 127482, doi:10.1016/j.molstruc.2019.127482.
[28] R.F.W. Bader, T.T. Nguyen-Dang, in: Advances in Quantum Chemistry Vol 14, Academic Press, Cambridge, 1981, p. 63.
[29] S. Harisha, J. Keshavayya, B.E. Kumara Swamy, C.C. Viswanath, Synthesis, characterization and electrochemical studies of azo dyes derived from barbituric acid, Dye. Pigment. 136 (2017) 742–753, doi:10.1016/j.dyepig.2016.09.004.
[30] H. Maqbool, S.D. Ganesh, U. Chandra, B.E. Kumaraswamy, V.K. Pai, Cyclic voltammetric studies of synthesized cardanol based azo dyes, Res. J. Chem. Sci. 3 (2013) 44–50.
[31] N. Menek, O. Çakir, H. Kocaokutgen, Polarographic and Voltammetric Behaviour of 2-Hydroxy-3-Tert-Butyl-5-Methylazobenzene, Mikrochim. Acta. 122 (1996) 203–207, doi:10.1007/BF01245783.
[32] N. Raju, A. Ramachandraiah, Spectral, electrochemical and molecular modeling studies of some 3-(2-hydroxy benzalhydrazino-4-thiazolyl)coumarins, E-Journal Chem 7 (2010) 583–592, doi:10.1155/2010/125972.
[33] M. Özkütük, E. Ipek, B. Aydiner, S. Mamaş, Z. Seferoılu, Synthesis, spectroscopic, thermal and electrochemical studies on thiazolyl azo based disperse dyes bearing coumarin, J. Mol. Struct. 1108 (2016) 521–532, doi:10.1016/j.molstruc.2015.12.032.
[34] J. Palion-Gazda, B. Machura, T. Klemens, A. Szlapa-Kula, S. Krompiec, M. Siwy, H. Janeczek, E. Schab-Balcerzak, J. Grzelak, S. Maćkowski, Structure-dependent and environment-responsive optical properties of the trisheterocyclic systems with electron donating amino groups, Dye. Pigment. 166 (2019) 283–300, doi:10.1016/j.dyepig.2019.03.035.
[35] K. Godugu, T.R. Gundala, R. Bodapati, V.D.S. Yadala, S.S. Loka, C.G.R. Nallagondu, Synthesis, photophysical and electrochemical properties of donor-acceptor type hydrazinyl thiazolyl coumarins, New J. Chem. 44 (2020) 7007–7016, doi:10.1039/d0nj00082e.
[36] Ö. Göktuğ, D. Akyüz, A. Koca, M.Kasım Şener, Synthesis and electropolymerization of EDOT modified 1,3-bis(5-methyl-2-thiazolylimino)isoindolinato palladium(II) complex for electrochemical detection of hydrogen peroxide, J. Coord. Chem. 70 (2017) 2052–2060, doi:10.1080/00958972.2017.1322695.
[37] S.Y. Ebrahimipour, I. Sheikhshoaie, J. Castro, W. Haase, M. Mohamadi, S. Foro, M. Sheikhshoaie, S. Esmaeili-Mahani, A novel cationic copper(II) Schiff base complex: synthesis, characterization, crystal structure, electrochemical evaluation, anti-cancer activity, and preparation of its metal oxide nanoparticles, Inorganica Chim. Acta. 430 (2015) 245–252, doi:10.1016/j.ica.2015.03.016.
[38] A. Caballero, V. Lloveras, D. Curiel, A. Tárraga, A. Espinosa, R. García, J. Vidal-Gancedo, C. Rovira, K. Wurst, P. Molina, J. Veciana, Electroactive thiazole derivatives capped with ferrocenyl units showing charge-transfer transition and selective ion-sensing properties: a combined experimental and theoretical study, Inorg. Chem. 46 (2007) 825–838, doi:10.1021/ic061803b.
[39] I. Sheikhshoaie, S.Y. Ebrahimipour, M. Sheikhshoaie, M. Mohamadi, M. Abbasnejad, H.A. Rudbari, G. Bruno, Synthesis, characterization, X-ray crystal structure, electrochemical evaluation and anti-cancer studies of a mixed ligand Cu(II) complex of (E)-N′-((2-hydroxynaphthalen-1-yl)methylene)acetohydrazide, J. Chem. Sci. 127 (2015) 2193–2200, doi:10.1007/s12039-015-0978-8.
[40] S. Biswas, A.K. Pramanik, T.K. Mondal, Palladium(II) complex with thiazole containing tridentate ONN donor ligand: synthesis, X-ray structure and DFT computation, J. Mol. Struct. 1088 (2015) 28–33, doi:10.1016/j.molstruc.2015.02.004.
[41] M. Krause, R. von der Stück, D. Brünink, S. Buss, N.L. Doltsinis, C.A. Strassert, A. Klein, Platinum and palladium complexes of tridentate −C^N^N (phen-ide)-pyridine-thiazol ligands – A case study involving spectroelectrochemistry, photoluminescence spectroscopy and TD-DFT calculations, Inorganica Chim. Acta. 518 (2021) 120093, doi:10.1016/j.ica.2020.120093.
[42] D. Hanahan, R.A. Weinberg, Hallmarks of cancer: the next generation, Cell 144 (2011) 646–674, doi:10.1016/j.cell.2011.02.013.
[43] C.C. Mills, E.A. Kolb, V.B. Sampson, Development of chemotherapy with cell cycle inhibitors for adult and pediatric cancer therapy, Cancer Res. 78 (2018) 320, doi:10.1158/0008-5472.CAN-17-2782.
[44] A. Saraste, K. Pulkki, Morphologic and biochemical hallmarks of apoptosis, Cardiovasc. Res. 45 (2000) 528–537, doi:10.1016/S0008-6363(99)00384-3.
[45] Y. Zhang, X. Chen, C. Gueydan, J. Han, Plasma membrane changes during programmed cell deaths, Cell Res. 28 (2017) 9–21, doi:10.1038/cr.2017.133.
[46] S. Elmore, Apoptosis: a review of programmed cell death, Toxicol. Pathol. 35 (2007) 495, doi:10.1080/01926230701320337.
[47] N. Prevarskaya, R. Skryma, Y. Shuba, Calcium signaling and apoptosis resistance of cancer cells, Appl. Apoptosis to Cancer Treat. (2005) 29–49.
[48] N. Prevarskaya, R. Skryma, Y. Shuba, Calcium in tumour metastasis: new roles for known actors, Nat. Rev. Cancer. 11 (2011) 609–618, doi:10.1038/nrc3105.
[49] A. Bergner, R. Huber, Regulation of the endoplasmic reticulum Ca(2+)-store in cancer, Anticancer. Agents Med. Chem. 8 (2008) 705–709, doi:10.2174/187152008785914734.
[50] A. Deniaud, O. Sharaf El Dein, E. Maillier, D. Poncet, G. Kroemer, C. Lemaire, C. Brenner, Endoplasmic reticulum stress induces calcium-dependent permeability transition, mitochondrial outer membrane permeabilization and apoptosis, Oncogene 27 (2007) 285–299, doi:10.1038/sj.onc.1210638.
[51] J.Y.J. Wang, DNA damage and apoptosis, Cell Death Differ 8 (2001) 1047–1048, doi:10.1038/sj.cdd.4400938.
[52] W.M. Bonner, C.E. Redon, J.S. Dickey, A.J. Nakamura, O.A. Sedelnikova, S. Solier, Y. Pommier, γH2AX and cancer, Nat. Rev. Cancer. 8 (2008) 957, doi:10.1038/NRC2523.